Article

Implementing Mesoporosity in Zeolitic Imidazolate Frameworks through Clip-Off Chemistry in Heterometallic Iron−Zinc ZIF-8

Luis León-Alcaide, Javier López-Cabrelles, María Esteve-Rochina, Enrique Ortí, Joaquín Calbo, Bas A. H. Huisman, Michele Sessolo, João C. Waerenborgh, Bruno J. C. Vieira, and Guillermo Mínguez Espallargas*

Read Online

ACCESS | Metrics & More | Article Recommendations | SI Supporting Information

ABSTRACT: Bond breaking has emerged as a new tool to postsynthetically modify the pore structure in metal−organic frameworks since it allows us to obtain pore environments in structures that are inaccessible by other techniques. Here, we extend the concept of clip-off chemistry to archetypical ZIF-8, taking advantage of the different stabilities of the bonds between imidazolate and Zn and Fe metal atoms in heterometallic Fe-Zn-ZIF-8. We demonstrate that Fe centers can be removed selectively without affecting the backbone of the structure that is supported by the Zn atoms. This allows us to create mesopores within the highly stable ZIF-8 structure. The strategy presented, combined with control of the amount of iron centers incorporated into the structure, permits porosity engineering of ZIF materials and opens a new avenue for designing novel hierarchical porous frameworks.

Fe-Zn-ZIF-8 → Hydrolysis → Activation → HP-Zn-ZIF-8
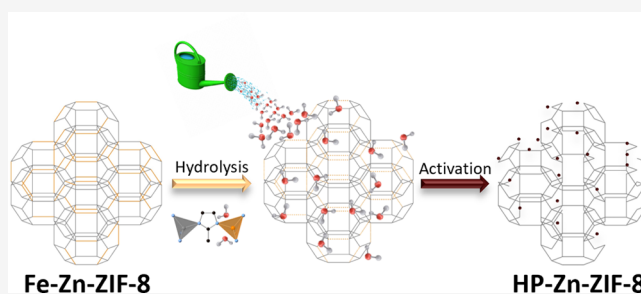
INTRODUCTION

Bond breaking in metal−organic frameworks (MOFs) is a pioneering manner to tune the physical properties of these porous materials.[1] This reticular design can be used to create open metal sites,[2−4] defect engineering,[5−10] and new morphologies,[11] or to carry out pore structure engineering.[12,13] The latter usage is especially interesting due to the possibility of creating hierarchical structures[14,15] by removing metal ions or linkers. This is achieved by randomly breaking some of the metal−ligand coordination bonds due to their low chemical or thermal stability,[16−18] as exemplified by water[19] or acid[20] etching, or by thermolysis.[21] Using this approach, however, it is difficult to precisely tune the pore sizes because of the absence of selectivity toward the chemical bonds that are targeted. An alternative manner to achieve discriminative cleavage has recently emerged, namely clip-off chemistry.[22] Clip-off chemistry is an innovative strategy to modify the connectivity in MOFs and is based on the use of a selective bond-breaking reaction to remove a controlled portion of the reticular network.[22] One of the overwhelming advantages of the clip-off approach is the meticulous control of the formation of mesoporous cavities, which can be achieved with different stimuli. Typically, this pore engineering approach is based on the different reactivity of the ligands to a specific process.[23−25] For example, Zhou and co-workers demonstrated the selective removal of ligands by exposing to ultraviolet laser a MOF containing both photolabile and robust ligands, thus creating a hierarchical structure upon elimination of the former.[26] A

controlled linker thermolysis or hydrolysis of a labile ligand can also be used to fuse micropores into mesopores.[27,28] On the other hand, Maspoch and co-workers reported ozonolysis as a successful way to cleave olefin bonds,[29,30] thus allowing the fusion of micropores to create mesopores. However, one limitation of these approaches is the necessity to incorporate specific reactive ligands or modulators in the structure of the MOF, which can become challenging to achieve in some archetypical families, such as zeolitic imidazolate frameworks (ZIFs).[31]

ZIFs are an important subclass of MOFs formed by tetrahedral metal centers (typically Zn^{2+} or Co^{2+}) linked by imidazolate ligands.[32−34] The archetypical member of this family is $Zn(mim)_2$ (mim = 2-methylimidazolate), commonly known as **ZIF-8**, which possesses a sodalite-type structure. We have recently reported the solvent-free preparation of the Fe^{2+} analogue of **ZIF-8**, namely **MUV-3**,[35] which is highly unstable toward exposure to water. Thus, we reasoned that the combination of stable Zn^{2+} centers with unstable Fe^{2+} centers in the same structure could yield a bimetallic **Fe-Zn-ZIF-8** with M−mim−M coordination bonds of different reactivity
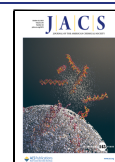
toward water molecules due to their different chemical behavior.[36] The application of clip-off chemistry on the coordination bond between the metal and the ligand is relatively unusual in MOF systems[37] and is applied here for the first time in ZIFs.

RESULTS AND DISCUSSION

The solvent-free reaction of a 1:1:4 mixture of ferrocene, zinc oxide, and 2-methylimidazole at 150 °C under vacuum results, after 96 h, in the formation of a yellow crystalline material of formula $Fe_{0.5}Zn_{0.5}(mim)_2$, denoted **Fe_{50}-Zn_{50}-ZIF-8**. Single-crystal X-ray diffraction analysis of the as-synthesized **Fe_{50}-Zn_{50}-ZIF-8** material reveals that the crystals are isostructural with **ZIF-8** and **MUV-3** (see Figure 1a), crystallizing in the
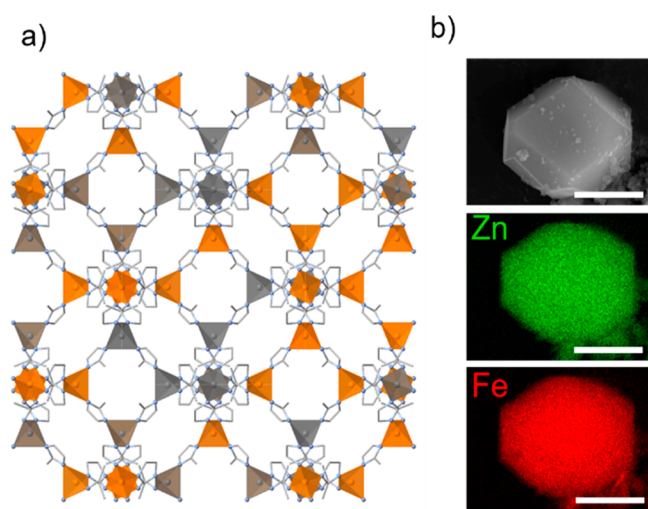
$I\bar{4}3m$ cubic space group with intermediate unit cell parameters ($a = 17.058$ Å, vs $a = 16.991$ Å in **ZIF-8** and $a = 17.165$ Å in **MUV-3**).[31,35] The typical morphology of **ZIF-8** crystals, i.e. truncated rhombic dodecahedron, is observed by scanning electron microscopy (SEM), as shown in Figure 1b and Figures S1–S5. The crystal structure is refined with a 50:50 Fe:Zn occupancy in the metal positions. Each metal center is connected to four nitrogen atoms from four imidazolate ligands, with bond distances between the pure counterparts (M–N distance of 2.033 Å and M···M distance of 6.031 Å in Fe_{50}-Zn_{50}-ZIF-8 vs 1.987 and 6.007 Å in ZIF-8 and 2.048 and 6.069 Å in MUV-3). The composition and the homogeneous distribution of metal centers are studied by energy dispersive X-ray spectroscopy (EDX) (see Table S1). These compositions are confirmed by inductively coupled plasma (ICP), and the presence of tetrahedrally coordinated Fe(II) was demonstrated by Mössbauer spectroscopy (see Table S2 and Figure S11). To confirm that all of the organic part of the heterometallic material corresponds to imidazolates, ^{1}H nuclear magnetic resonance (^{1}H NMR) was carried out, unequivocally identifying the protons of the mim ligands (see Figure S12).

The Fe:Zn ratio in **Fe-Zn-ZIF-8** can be modified by tuning the starting composition, as exemplified by five different isostructural samples, namely **Zn-ZIF-8** (i.e., ZIF-8 with 100% Zn^{2+}), **Fe_{25}-Zn_{75}-ZIF-8**, **Fe_{50}-Zn_{50}-ZIF-8**, **Fe_{75}-Zn_{25}-ZIF-8**, and **Fe_{100}-ZIF-8** (i.e., MUV-3 with 100% Fe^{2+}). The powder X-ray diffraction (PXRD) patterns of the samples of **Fe-Zn-ZIF-8** in different proportions reveal the same powder diffractogram that was used in the case of the pure counterparts (Figure 2a). However, the peaks are slightly shifted to lower 2θ values as the amount of Fe^{2+} increases, indicative of an increase in the size of the unit cell axis of the framework (see Figure 2b and Table S4).

N_2 sorption isotherms of the different bimetallic materials (Figure 2c) show a reduction of the accessible surface area calculated using the Brunauer–Emmett–Teller (BET) model in comparison with the pure homometallic ZIFs. Thus, values of 785, 620, and 515 m^2 g^{-1} are calculated for **Fe_{25}-Zn_{75}-ZIF-8**, **Fe_{50}-Zn_{50}-ZIF-8**, and **Fe_{75}-Zn_{25}-ZIF-8**, respectively, whereas **Zn_{100}-ZIF-8** and **Fe_{100}-ZIF-8** have BET values of 1455 and 960 m^2 g^{-1}, respectively. The pore size distribution was

Figure 1. (a) Crystal structure of **Fe_{50}-Zn_{50}-ZIF-8**. Note that the distribution of the Fe (orange tetrahedra) and Zn (gray tetrahedra) centers in the figure has been assigned arbitrarily to indicate a 50:50 random distribution. In the single-crystal X-ray data, however, the metal centers cannot be distinguished and have been refined in the same crystallographic position. (b) SEM image of the **Fe_{50}-Zn_{50}-ZIF-8** truncated rhombic dodecahedron and its corresponding elemental mapping of zinc and iron (scale bars = 5 μm).
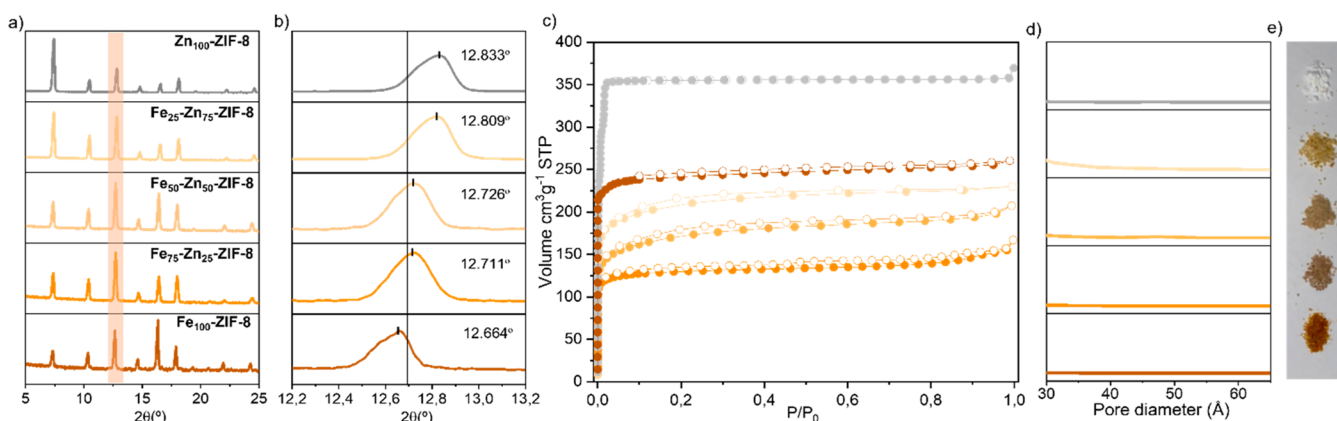

Figure 2. (a) PXRD diffractogram of **Fe-Zn-ZIF-8** with different ratios of Fe:Zn. (b) Zoom into the peak between $2\theta = 12.2$ and $13.2°$ to study the shifting caused by the incorporation of two different metal ions in the same structure. The shifting is compared to the pristine counterparts (bottom and top curves). The thin black line at $2\theta = 12.7°$ is included to facilitate the comparison of the position of the peaks. (c) N_2 sorption isotherms at 77 K (solid circles for sorption and open circles for desorption) of **Fe-Zn-ZIF-8** with different ratios of Fe:Zn. (d) Pore size distribution estimated by BJH of the same materials. (e) Images of the progressive change of color in the different **Fe-Zn-ZIF-8** materials.

calculated from Barrett−Joyner−Halenda (BJH) analysis (Figure 2d), indicating the absence of mesoporous cavity formation in all cases. The presence of two different types of ions forming the pore window might affect the breathing and flexibility of the net, making it much more rigid or causing a suppression of the gate opening, which would lead to a decrease in the adsorption capacity of the material. However, theoretical calculations under the density functional theory (DFT) framework (HSE06 level of theory; see computational details in the Supporting Information) estimate a gate opening energy penalty of 6.54 and 2.89 kJ mol^{-1} per linker for Zn_{100}-ZIF-8 and Fe_{100}-ZIF-8, respectively, in line with recently reported data,[38] whereas intermediate values are predicted for Fe_{50}-Zn_{50}-ZIF-8 (2.8−4.4 kJ mol^{-1} per linker). Note also the limitations that have been raised recently in BET theory when applied to heterogeneous surfaces.[39] The N_2 quadrupole moment may cause an orienting effect on highly polar frameworks, and indeed we predict strong electrostatic polarization (and therefore different N_2 affinity) in going from Zn_{100}-ZIF-8 to Fe_{100}-ZIF-8 and to Fe_{50}-Zn_{50}-ZIF-8 (especially in the secondary building unit environment; Figure S26).

The increase in the amount of iron in the structure is also accompanied by a change in the color of the bimetallic material, from the characteristic white of ZIF-8 to the orange of MUV-3, with different tones of yellow-orange (see Figure 2e). As both reference compounds (ZIF-8 and MUV-3) have been reported to be direct bandgap semiconductors,[38] the color change observed in the bulk solid might indicate a narrowing of the bandgap when substituting Zn^{2+} by Fe^{2+}. In order to shed light on the color change, we measured the optical reflectance of the pure iron compound (Fe_{100}-ZIF-8, or MUV-3) and of the bimetallic material with equimolar amounts of Zn^{2+} and Fe^{2+} (Fe_{50}-Zn_{50}-ZIF-8). We did not characterize the Zn_{100}-ZIF-8 material, as its bandgap, reported to be ca. 5 eV,[40] is too high to be accessible with our UV−Vis lamp and spectrometer. As can be seen from Figure 3a, Fe_{100}-ZIF-8 is strongly absorbing in the UV-blue part of the electromagnetic spectrum (2.6−3.5 eV, corresponding to approximately 350−475 nm) and shows a steep reduction of the optical absorption in the 2.2−2.6 eV region, likely due to bandgap transitions. A very similar absorption profile is found for the bimetallic Fe_{50}-Zn_{50}-ZIF-8 compound, which shows, however, a depletion of the optical absorption at approximately 3.2 eV. At lower photon energies, both materials exhibit low absorption and become gradually transparent in the red-NIR region. These simple measurements suggest an optical bandgap of approximately 2.4 eV for both Fe_{100}-ZIF-8 and Fe_{50}-Zn_{50}-ZIF-8, as estimated by the first derivative of the spectra. Note that a precise determination of the bandgap is hindered by the fact that the absorption profiles are not very steep. This observation might indicate a (partially) indirect character of the band-to-band transition in this class of compounds or the presence of local defects/impurities. Noteworthy, the reflectance data contrast with previous calculations, which placed the bandgap of the Fe_{100}-ZIF-8 compound at ca. 3.4 eV,[38] significantly shifted to higher energies compared to our optical experiments.

First-principles calculations in periodic boundary conditions were performed under the DFT approach to understand the optical properties of Zn_{100}-ZIF-8, Fe_{100}-ZIF-8, and Fe_{50}-Zn_{50}-ZIF-8 (see the Supporting Information for full computational details). First, the minimum-energy crystal structure of the ZIF
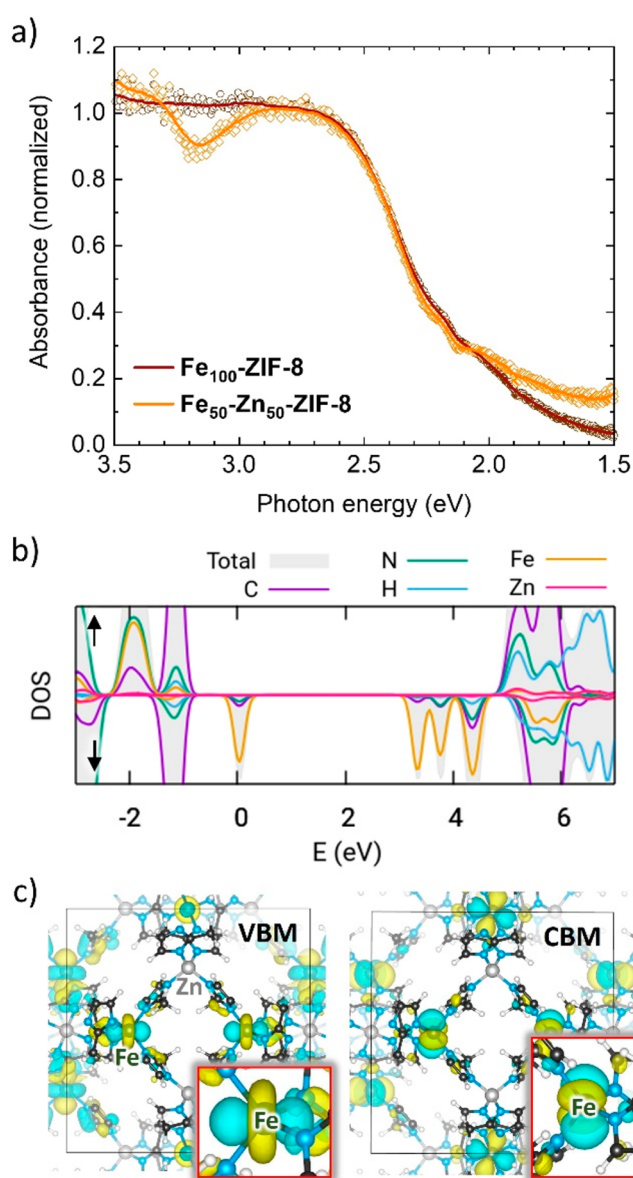

Figure 3. (a) Optical absorbance spectra estimated by reflectance measurements of Fe_{100}-ZIF-8 and Fe_{50}-Zn_{50}-ZIF-8. The spectra were normalized at 2.7 eV to make their comparison. (b) Species-projected density of states (spin-up and spin-down channels) calculated at the HSE06 level of theory for Fe_{50}-Zn_{50}-ZIF-8 (alternating Zn/Fe configuration and ferromagnetic alignment). The electronic bandgap is calculated at 3.30 eV. (c) Crystal orbital topology of the valence band maximum (VBM) and conduction band minimum (CBM) (spin-down channel).

materials was obtained upon full ionic and lattice relaxation at the PBEsol level without symmetry constraints. The optimized lattice parameters (Table S6) are in good accordance with those previously reported for Zn_{100}-ZIF-8 and Fe_{100}-ZIF-8,[41] and suggest a slightly larger pore size in the Fe(II)-based material. Fe_{50}-Zn_{50}-ZIF-8 was modeled in up to 5 configurations taking into account the metal (Fe/Zn) spatial distribution of the secondary building unit (SBU) in the framework (see Figure S21). A small energy difference was predicted between them (<0.04 eV), and the unit cell size was calculated to be intermediate between those of the pure materials (Table S6), in agreement with the experimental single-crystal data. Band structure calculations at the HSE06
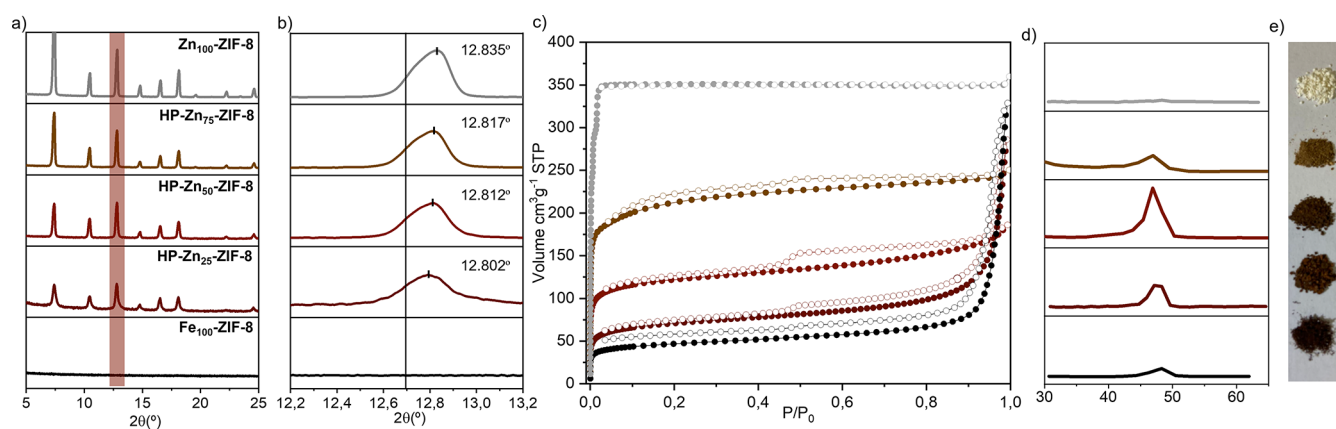
Figure 4. (a) PXRD diffractogram of **HP-Zn-ZIF-8** with different ratios of Fe:Zn. (b) Zoom into the peak between $2\theta = 12.2$ and 13.2 to study the shift caused by removing the tetrahedral iron centers from the **ZIF-8** backbone. The shift is compared with that of the counterparts after the hydrolysis process. The thin black line at $2\theta = 12.7°$ is included to facilitate the comparison of the position of the peaks. (c) N_2 sorption isotherms at 77K (solid circles for sorption and open circles for desorption) of **HP-Zn-ZIF-8** with different ratios of Fe:Zn. (d) Pore size distribution estimated by BJH of the same materials. (e) Images of the progressive change of color in the different **HP-Zn-ZIF-8** materials.

level indicate that the bandgap nature of **Zn$_{100}$-ZIF-8** is described by a valence band maximum (VBM) and a conduction band minimum (CBM) localized on the imidazole organic ligand (Figures S22 and S23), with a direct bandgap (E_g) estimation of 5.44 eV. This value is in good accord with that reported by Walsh et al. (5.3 eV).[42] In contrast, the bandgap of **Fe$_{100}$-ZIF-8** is governed by Fe(II) $d \rightarrow d$ electronic transitions (Figures S22 and S23). In a first approach, it is calculated to have a value of 3.36 eV, in line with the work of Vitillo et al. (3.4 eV),[38] but in sharp contrast to our optical measurements (2.4 eV, Figure 3a). Similarly, the bandgap of the bimetallic framework is predicted to originate at the Fe(II) SBU (Figure 3b and c), with an E_g ranging 3.30–3.53 eV for the different configurations modeled for **Fe$_{50}$-Zn$_{50}$-ZIF-8** (Figure S25).

Theoretical bandgap estimations based on the energy difference between the VBM and the CBM (i.e., the fundamental bandgap) usually compares well with the optical bandgap when the exciton is delocalized over a relatively medium-to-large entity (small exciton binding energy, E_{bind}), such as the imidazole ligand in **Zn$_{100}$-ZIF-8**. However, strong E_{bind} values of the order of 1 eV are expected in electronic transitions involving highly confined excitons, as is the case of Fe(II)-centered $d \rightarrow d$ excitations in **Fe$_{100}$-ZIF-8** and **Fe-Zn-ZIF-8**. To take into account the electronic stabilization due to the hole and electron pairing upon excitation, we computed the exciton binding energy of the imidazole-centered excitation and compared it with that calculated for the Fe(II)-based SBU transition, using a Frenkel exciton approach (see the Supporting Information for details). Theoretical calculations predict a E_{bind} of 0.29 eV for imidazole, which results in an optical E_g of 5.15 eV for **Zn$_{100}$-ZIF-8** in good correlation with experimentally reported bandgap of 4.9 eV.[40] In contrast, a larger exciton binding energy of 0.76 eV is predicted for the Fe(II)-centered excitation, which upon subtraction from the fundamental bandgap results in an optical E_g of 2.60 eV for **Fe$_{100}$-ZIF-8** and 2.54–2.84 eV for **Fe$_{50}$-Zn$_{50}$-ZIF-8**. These results nicely correlate with the steep increase in the absorption signal recorded in the optical experiments for **Fe$_{100}$-ZIF-8** and **Fe$_{50}$-Zn$_{50}$-ZIF-8** at *ca.* 2.4 eV, and with the absorption maximum recorded at 2.7 eV for the latter (Figure 3a).

Importantly, the different composition of bimetallic **Fe-Zn-ZIF-8** has a direct effect on the stability of the structure in air. Thus, upon exposing **Zn-ZIF-8**, **Fe$_{25}$-Zn$_{75}$-ZIF-8**, and **Fe$_{50}$-Zn$_{50}$-ZIF-8** to air, no significant structural change is observed in the PXRD. On the contrary, a significant loss of crystallinity is observed after exposure of **Fe$_{75}$-Zn$_{25}$-ZIF-8** and **Fe$_{100}$-ZIF-8** to air, as seen in the PXRD data (Figure S27). The origin of this structural collapse is the instability of the Fe(II) ion in the presence of atmospheric water molecules. To assess the different metal-imidazole bond stability, first-principles calculations were performed by means of topological analysis of the HSE06 electron density on relevant bond strength indexes, such as the Wiberg bond index (WBI), the natural atomic orbital (NAO) bond order, and the intrinsic bond strength index (IBSI) (see the Supporting Information for details). Theoretical calculations predict smaller WBI, NAO, and IBSI values for the Fe−N bond (Table S7), as well as half bond breaking energy (Figure S28), confirming its weaker strength and therefore its more unstable nature, compared to the Zn−N bond. The higher polarity predicted in the electrostatic maps of Fe(II)-containing ZIFs (Figure S26) further supports the lower air stability toward water or moisture.[35,44] Moreover, we have recently reported a new Fe-ZIF material (**MUV-24**) that has a reduced melting temperature compared with the Zn analogue.[43]

These results prompted us to explore a controlled way to eliminate the iron centers while retaining the structural integrity through the zinc centers, i.e., by applying the concepts of clip-off chemistry to the metal centers. Specifically, the more labile Fe(II) ions are removed through hydrolysis.

The controlled hydrolysis process was carried out by two different procedures: (i) by leaving the heterometallic **Fe-Zn-ZIF-8** exposed to the air for several days, and (ii) by introducing the heterometallic **Fe-Zn-ZIF-8** in water and stirring for 1 h. Both procedures were followed by heating the material at 90 °C for 4 h, washing with fresh acetonitrile several times, and drying under vacuum. Hydrolysis causes no changes in the backbone of the material, which is easily corroborated by PXRD (Figure 4). Close inspection of the PXRD reveals that not only is the sodalite structure maintained upon the clip-off protocol but also the peaks are displaced to higher 2θ values (compare Figure 4a and b with Figure 2a and

b and Table S4), consistent with the unit cell of pure Zn_{100}-ZIF-8. This results from the elimination of the iron centers from the structure, which now contains exclusively zinc centers, forming a new subclass of hierarchical porous materials named **HP-Zn-ZIF-8**. In addition, upon increasing the content of iron in the parent material, a significant decrease in the intensity of the peaks is also observed: i.e., a decrease in the crystallinity caused by the lack of enough Zn centers that can support the sodalite structure. This loss of crystallinity is complete in the case of Fe_{100}-ZIF-8 (i.e., **MUV-3**), leading to a total collapse of the crystalline structure (Figure 4a).

SEM measurements confirm the preservation of the crystal morphology upon the clip-off of the iron centers (Figure 5a, b
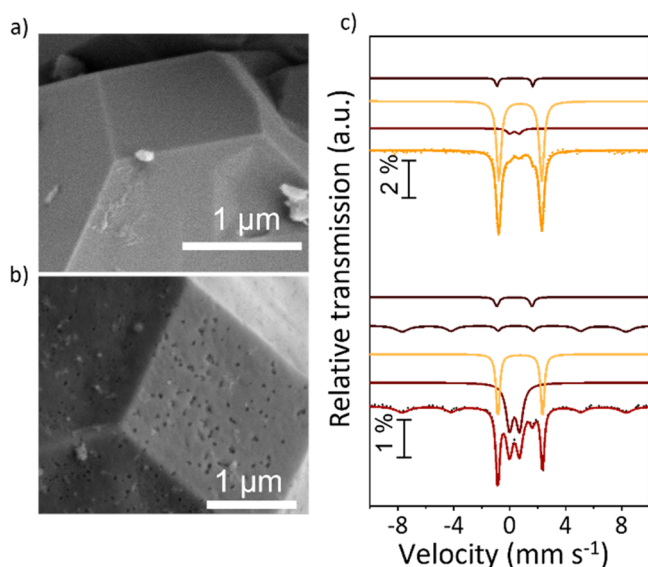

Figure 5. (a) SEM image of as-synthesized Fe_{50}-Zn_{50}-ZIF-8. (b) SEM image of **HP-Zn$_{50}$-ZIF-8**. (c) Mössbauer spectra of as-synthesized Fe_{50}-Zn_{50}-ZIF-8 (top) and **HP-Zn$_{50}$-ZIF-8** (bottom).

and Figure S10). However, EDX shows a homogeneous distribution of both ions along the solid (Figure S9), which demonstrates that the extruded iron centers are not completely removed from the solid but displaced to the pores of the structure.

The Mössbauer spectrum of the as-synthesized Fe_{50}-Zn_{50}-ZIF-8 (Figure 5c-top) shows a quadrupole doublet with isomer shift and quadrupole splitting, typical of tetracoordinated Fe^{2+}, spin $S = 4$ (see Table S2),[45] which is consistent with Fe^{2+} occupying the Zn^{2+} sites of the sodalite structure. Two very low intensity doublets assigned to Fe^{3+} are also observed.[46] After the hydrolysis of Fe_{50}-Zn_{50}-ZIF-8 to generate **HP-Zn$_{50}$-ZIF-8**, the Mössbauer spectrum (Figure 5c-bottom) shows that the Fe^{3+} doublet with the lowest splitting has grown at the expense of the relative area of the Fe^{2+} doublet. Furthermore, a sextet typical of Fe^{3+} ($S = 5/2$) in Fe oxides can also be observed, corresponding to superparamagnetic Fe oxides.[47] This assignment is confirmed by the spectra taken at 4 K (Figure S11c), below the blocking temperature, thus revealing a distribution of sizes of the oxide nanoparticles, the largest ones showing a blocking temperature similar to or higher than 80 K. The Mössbauer data therefore indicate that a first oxidation step of the Fe^{2+} ion initially occurs, with the generated Fe^{3+} being part of the sodalite structure on a very distorted site, giving rise to the Fe^{3+} doublet

with high quadrupole splitting. As the material is further oxidized, this unstable Fe^{3+} species forms nanosized superparamagnetic oxides that remain in the pores generated by the removal of the Fe^{2+} centers. Their presence is consistent with the fact that the samples can be moved by a magnet after a while in air at room temperature. It should be noted that the two processes, metal–ligand bond cleavage and oxidation of the iron centers, are combined in the global process of mesopore formation. However, previous results on MUV-3 have shown that the material exhibits notable stability under a dry O_2 atmosphere but quickly degrades under the presence of water.[35]

After the hydrolysis process, the formation of hierarchical pore structures is straightforwardly characterized by N_2 adsorption. Figure 4c shows the N_2 adsorption of the different **HP-Zn-ZIF-8** materials. A decrease in the microporous adsorption is observed as the amount of iron increases, likely due to a larger content of iron oxide within the pores (Table S5). Importantly, a hysteresis is observed at relatively high pressures ($P/P_0 > 0.4$), which is more evident with an increased amount of structural iron in the parent compound, confirming the presence of mesopores. This is further supported by BJH pore size analysis, which illustrates mesopore formation in the pore size distribution upon hydrolysis of the materials (Figure 4d). Initially all of the porosity belongs to microporosity, whereas macroporosity partially replaces the microporosity upon the etching process of the labile Fe^{2+} centers.

CONCLUSIONS

In conclusion, clip-off chemistry is used to create mesopores in sodalite structures by taking advantage of the different stabilities of the metal ions that make up the structure in bimetallic zeolitic imidazole frameworks. In particular, we report the synthesis of bimetallic **Fe-Zn-ZIF-8** materials, where Fe–N bonds are much more susceptible to hydrolysis than Zn–N bonds. In this way, the imidazolates coordinated to the iron atoms can be selectively removed, maintaining the crystalline structure of the material that is supported by the Zn atoms, thus producing a hierarchical porous ZIF-8, denoted as **HP-Zn$_x$-ZIF-8**, with both micro- and mesopores. Mesoporosity depends directly on the proportions of each ion in the structure, so the resulting **HP-Zn$_x$-ZIF-8** can be rationally tuned by the relative content of Fe(II). The clip-off approach reported herein is expected to be applicable to other materials in which ions showing different bond strengths can be incorporated, thus allowing precise control toward defect engineering.

EXPERIMENTAL SECTION

Synthesis of MUV-3 (Fe_{100}-ZIF-8). Ferrocene (30 mg, 0.16 mmol), 2-methylimidazole (25 mg, 0.32 mmol), and 4,4′-bipyridine as a template (50 mg, 0.32 mmol) were combined and sealed under vacuum in a layering tube (4 mm diameter). The mixture was heated to 150 °C for 4 days. The product was cooled to room temperature, and the layering tube was then opened. The unreacted precursors were extracted with acetonitrile and benzene, and **MUV-3** was isolated as yellow crystals. Phase purity was established by powder X-ray powder diffraction.

Synthesis of Fe-Zn-ZIF-8. A mixture of ferrocene, ZnO, and 2-methylimidazole (25 mg, 0.32 mmol) was combined and sealed under vacuum in a layering tube (4 mm diameter). The mixture was heated at 150 °C for 4 days. The product was allowed to cool to room temperature, and the layering tube was then opened. The unreacted

precursors were extracted with acetonitrile and benzene, and **Fe$_{100-x}$-Zn$_x$-ZIF-8** was isolated with different shades of yellow crystals (depending of the proportion of each metal). Phase purity was established by X-ray powder diffraction.

Single Crystal Diffraction. A single crystal of **Fe$_{50}$-Zn$_{50}$-ZIF-8** was mounted on a glass fiber by using a viscous hydrocarbon oil to coat the crystal and then transferred directly to the cold nitrogen stream for data collection. X-ray data were collected on a Supernova diffractometer equipped with a graphite-monochromated enhanced (Mo) X-ray source ($\lambda = 0.71073$ Å). Data were measured using the CrysAlisPro suite of programs. The program CrysAlisPro, Rigaku, was used for unit cell determinations and data reduction. Empirical absorption correction was performed using spherical harmonics, implemented in the SCALE3 ABSPACK scaling algorithm, based upon symmetry-equivalent reflections combined with measurements at different azimuthal angles. The crystal structures were solved and refined against all F^2 values using the SHELXL and Olex2 suite of programs.[48,49] Atomic displacement parameters of all non-hydrogen atoms were refined anisotropically. Hydrogen atoms were placed in calculated positions, refined using idealized geometries (riding model), and assigned fixed isotropic atomic displacement parameters.

Powder X-ray Diffraction. Polycrystalline samples of pure and mixed-metal **Fe$_{100-x}$-Zn$_x$-ZIF-8** ZIFs (prepared by solvent-free synthesis) were lightly ground in an agate mortar and pestle and used to fill 0.7 mm borosilicate capillaries that were mounted and aligned on an Empyrean PANalytical powder diffractometer, using Cu Kα radiation ($\lambda = 1.54056$ Å). Three repeated measurements were collected at room temperature ($2\theta = 5-40°$) and merged in a single diffractogram for each sample, with sharp and intense peaks denoting the high crystallinity of the material. Pawley refinements were performed using TOPAS 6.0.[50]

N$_2$ Gas Sorption. Single-gas N$_2$ volumetric isotherms were carried out in a Tristar II Plus (Micromeritics) at 77 K. 50 mg of the thoroughly washed with acetonitrile **Fe$_{100-x}$-Zn$_x$-ZIF-8** and **HP-Zn-ZIF-8** were activated at 200 °C for 2 h under vacuum. The BET surface area was calculated by using the BET equation, and the micropore volume was calculated by the desorption BJH analysis.

Mössbauer Spectroscopy. Mössbauer spectra were collected at 80 and at 4 K in transmission mode using a conventional constant-acceleration spectrometer and a 25 mCi ^{57}Co source in a Rh matrix. The velocity scale was calibrated by using α-Fe foil. Isomer shifts (IS) are given relative to these standards at room temperature. The absorbers were obtained by packing the powdered samples in a perspex holder. The absorber thickness was calculated on the basis of the corresponding electronic mass-absorption coefficients for the 14.4 keV radiation.[51] The low temperature spectra were collected in a bath cryostat with the sample immersed in liquid He at 4 K or in He exchange gas at 80 K. The spectra were fitted to Lorentzian lines using a nonlinear least-squares method.

Optical Absorption. UV−visible absorption spectra of the materials in powder form were collected with an Avantes setup integrated in a nitrogen-filled glovebox. The setup consists of a reflection integrating sphere (AvaSphere-50) coupled to a fiber-optics Avaspec-2048 spectrometer and a deuterium/halogen lamp (Ava-Light-DH-S). The powders were gently pressed between two quartz substrates and placed below the aperture of the integrating sphere.

Theoretical Calculations. First-principles calculations were performed under the DFT framework by means of the FHI-aims software package using periodic boundary conditions.[52] The minimum-energy crystal structures were obtained upon full ionic and lattice relaxation at the PBEsol level of theory without symmetry constraints.[53] High-level single-point calculations on the electronic structure were performed by means of the hybrid HSE06 functional[54] and the "really tight" numerical-centered atomic orbital (NAO) basis set. Up to five **Fe$_{50}$-Zn$_{50}$-ZIF-8** materials were modeled with different Zn/Fe SBU distribution (see the Supporting Information). Exciton binding energies were estimated in a cluster approach through a Frenkel exciton framework.[55,56] Gate opening energy penalties were obtained by simulating the open-gate phase by tilting the imidazolate dihedral angles along the N−N vector in a parallel fashion. Bond strength indexes were calculated in a cluster approximation of the SBU by using the Gaussian 16.A03 suite of programs[57] and IGMPlot.[58]

■ ASSOCIATED CONTENT

Ⓢ Supporting Information

The Supporting Information is available free of charge at https://pubs.acs.org/doi/10.1021/jacs.3c08017.

> General methods, materials, crystallographic data, characterization details, computational details, and supporting theoretical data (PDF)

Accession Codes

CCDC 2281602 contains the supplementary crystallographic data for this paper. These data can be obtained free of charge via www.ccdc.cam.ac.uk/data_request/cif, or by emailing data_request@ccdc.cam.ac.uk, or by contacting The Cambridge Crystallographic Data Centre, 12 Union Road, Cambridge CB2 1EZ, UK; fax: +44 1223 336033.

■ AUTHOR INFORMATION

Corresponding Author

Guillermo Mínguez Espallargas − *Instituto de Ciencia Molecular (ICMol), Universidad de Valencia, Paterna 46980, Spain;* Ⓞ orcid.org/0000-0001-7855-1003; Email: guillermo.minguez@uv.es

Authors

Luis León-Alcaide − *Instituto de Ciencia Molecular (ICMol), Universidad de Valencia, Paterna 46980, Spain*

Javier López-Cabrelles − *Instituto de Ciencia Molecular (ICMol), Universidad de Valencia, Paterna 46980, Spain;* Ⓞ orcid.org/0000-0001-7443-4635

María Esteve-Rochina − *Instituto de Ciencia Molecular (ICMol), Universidad de Valencia, Paterna 46980, Spain*

Enrique Ortí − *Instituto de Ciencia Molecular (ICMol), Universidad de Valencia, Paterna 46980, Spain;* Ⓞ orcid.org/0000-0001-9544-8286

Joaquín Calbo − *Instituto de Ciencia Molecular (ICMol), Universidad de Valencia, Paterna 46980, Spain;* Ⓞ orcid.org/0000-0003-4729-0757

Bas A. H. Huisman − *Instituto de Ciencia Molecular (ICMol), Universidad de Valencia, Paterna 46980, Spain;* Ⓞ orcid.org/0000-0002-3553-3398

Michele Sessolo − *Instituto de Ciencia Molecular (ICMol), Universidad de Valencia, Paterna 46980, Spain;* Ⓞ orcid.org/0000-0002-9189-3005

João C. Waerenborgh − *Centro de Ciências e Tecnologias Nucleares, DECN, Instituto Superior Técnico, Universidade de Lisboa, Bobadela LRS 2695-066, Portugal*

Bruno J. C. Vieira − *Centro de Ciências e Tecnologias Nucleares, DECN, Instituto Superior Técnico, Universidade de Lisboa, Bobadela LRS 2695-066, Portugal*

Complete contact information is available at:
https://pubs.acs.org/10.1021/jacs.3c08017

Notes

The authors declare no competing financial interest.

■ REFERENCES

(1) Zhou, X.; Jin, H.; Xia, B. Y.; Davey, K.; Zheng, Y.; Qiao, S.-Z. Molecular Cleavage of Metal-Organic Frameworks and Application to Energy Storage and Conversion. *Adv. Mater.* **2021**, *33*, No. 2104341.

(2) Kim, H. K.; Yun, W. S.; Kim, M. B.; Kim, J. Y.; Bae, Y. S.; Lee, J. D.; Jeong, N. C. A Chemical Route to Activation of Open Metal Sites in the Copper-Based Metal-Organic Framework Materials HKUST-1 and Cu-MOF-2. *J. Am. Chem. Soc.* **2015**, *137*, 10009−10015.

(3) Espín, J.; Garzón-Tovar, L.; Carné-Sánchez, A.; Imaz, I.; Maspoch, D. Photothermal Activation of Metal-Organic Frameworks Using a UV-Vis Light Source. *ACS Appl. Mater. Interfaces* **2018**, *10*, 9555−9562.

(4) Schlichte, K.; Kratzke, T.; Kaskel, S. Improved Synthesis, Thermal Stability and Catalytic Properties of the Metal-Organic Framework Compound Cu$_3$(BTC)$_2$. *Microporous Mesoporous Mater.* **2004**, *73*, 81−88.

(5) Vermoortele, F.; Bueken, B.; Le Bars, G.; Van De Voorde, B.; Vandichel, M.; Houthoofd, K.; Vimont, A.; Daturi, M.; Waroquier, M.; Van Speybroeck, V.; Kirschhock, C.; De Vos, D. E. Synthesis Modulation as a Tool to Increase the Catalytic Activity of Metal-Organic Frameworks: The Unique Case of UiO-66(Zr). *J. Am. Chem. Soc.* **2013**, *135*, 11465−11468.

(6) Dissegna, S.; Epp, K.; Heinz, W. R.; Kieslich, G.; Fischer, R. A. Defective Metal-Organic Frameworks. *Adv. Mater.* **2018**, *30*, No. 1704501.

(7) Song, D.; Bae, J.; Ji, H.; Kim, M. B.; Bae, Y. S.; Park, K. S.; Moon, D.; Jeong, N. C. Coordinative Reduction of Metal Nodes Enhances the Hydrolytic Stability of a Paddlewheel Metal-Organic Framework. *J. Am. Chem. Soc.* **2019**, *141*, 7853−7864.

(8) Feng, X.; Hajek, J.; Jena, H. S.; Wang, G.; Veerapandian, S. K. P.; Morent, R.; De Geyter, N.; Leyssens, K.; Hoffman, A. E. J.; Meynen, V.; Marquez, C.; De Vos, D. E.; Van Speybroeck, V.; Leus, K.; Van Der Voort, P. Engineering a Highly Defective Stable UiO-66 with Tunable Lewis-Brønsted Acidity: The Role of the Hemilabile Linker. *J. Am. Chem. Soc.* **2020**, *142*, 3174−3183.

(9) Shearer, G. C.; Chavan, S.; Bordiga, S.; Svelle, S.; Olsbye, U.; Lillerud, K. P. Defect Engineering: Tuning the Porosity and Composition of the Metal-Organic Framework UiO-66 via Modulated Synthesis. *Chem. Mater.* **2016**, *28*, 3749−3761.

(10) Wu, H.; Chua, Y. S.; Krungleviciute, V.; Tyagi, M.; Chen, P.; Yildirim, T.; Zhou, W. Unusual and Highly Tunable Missing-Linker Defects in Zirconium Metal-Organic Framework UiO-66 and Their Important Effects on Gas Adsorption. *J. Am. Chem. Soc.* **2013**, *135*, 10525−10532.

(11) Zhou, X.; Dong, J.; Zhu, Y.; Liu, L.; Jiao, Y.; Li, H.; Han, Y.; Davey, K.; Xu, Q.; Zheng, Y.; Qiao, S. Z. Molecular Scalpel to Chemically Cleave Metal-Organic Frameworks for Induced Phase Transition. *J. Am. Chem. Soc.* **2021**, *143*, 6681−6690.

(12) Feng, L.; Day, G. S.; Wang, K. Y.; Yuan, S.; Zhou, H. C. Strategies for Pore Engineering in Zirconium Metal-Organic Frameworks. *Chem.* **2020**, *6*, 2902−2923.

(13) Albolkany, M. K.; Liu, C.; Wang, Y.; Chen, C. H.; Zhu, C.; Chen, X.; Liu, B. Molecular Surgery at Microporous MOF for Mesopore Generation and Renovation. *Angew. Chem., Int. Ed.* **2021**, *60*, 14601−14608.

(14) Huang, H.; Li, J. R.; Wang, K.; Han, T.; Tong, M.; Li, L.; Xie, Y.; Yang, Q.; Liu, D.; Zhong, C. An in Situ Self-Assembly Template Strategy for the Preparation of Hierarchical-Pore Metal-Organic Frameworks. *Nat. Commun.* **2015**, *6*, 8847.

(15) DeCoste, J. B.; Rossin, J. A.; Peterson, G. W. Hierarchical Pore Development by Plasma Etching of Zr-Based Metal−Organic Frameworks. *Chem.—Eur. J.* **2015**, *21*, 18029−18032.

(16) Qi, S. C.; Qian, X. Y.; He, Q. X.; Miao, K. J.; Jiang, Y.; Tan, P.; Liu, X. Q.; Sun, L. B. Generation of Hierarchical Porosity in Metal−Organic Frameworks by the Modulation of Cation Valence. *Angew. Chem., Int. Ed.* **2019**, *58*, 10104−10109.

(17) Jeong, G. Y.; Singh, A. K.; Kim, M. G.; Gyak, K. W.; Ryu, U. J.; Choi, K. M.; Kim, D. P. Metal-Organic Framework Patterns and Membranes with Heterogeneous Pores for Flow-Assisted Switchable Separations. *Nat. Commun.* **2018**, *9*, 3968.

(18) Chen, S.; Song, Z.; Lyu, J.; Guo, Y.; Lucier, B. E. G.; Luo, W.; Workentin, M. S.; Sun, X.; Huang, Y. Anhydride Post-Synthetic Modification in a Hierarchical Metal-Organic Framework. *J. Am. Chem. Soc.* **2020**, *142*, 4419−4428.

(19) Kim, Y.; Yang, T.; Yun, G.; Ghasemian, M. B.; Koo, J.; Lee, E.; Cho, S. J.; Kim, K. Hydrolytic Transformation of Microporous Metal-Organic Frameworks to Hierarchical Micro- and Mesoporous MOFs. *Angew. Chem., Int. Ed.* **2015**, *54*, 13273−13278.

(20) Koo, J.; Hwang, I. C.; Yu, X.; Saha, S.; Kim, Y.; Kim, K. Hollowing out MOFs: Hierarchical Micro- and Mesoporous MOFs with Tailorable Porosity via Selective Acid Etching. *Chem. Sci.* **2017**, *8*, 6799−6803.

(21) Chen, S.; Mukherjee, S.; Lucier, B. E. G.; Guo, Y.; Wong, Y. T. A.; Terskikh, V. V.; Zaworotko, M. J.; Huang, Y. Cleaving Carboxyls: Understanding Thermally Triggered Hierarchical Pores in the Metal-Organic Framework MIL-121. *J. Am. Chem. Soc.* **2019**, *141*, 14257−14271.

(22) Yang, Y.; Broto-Ribas, A.; Ortín-Rubio, B.; Imaz, I.; Gándara, F.; Carné-Sánchez, A.; Guillerm, V.; Jurado, S.; Busqué, F.; Juanhuix, J.; Maspoch, D. Clip-off Chemistry: Synthesis by Programmed Disassembly of Reticular Materials. *Angew. Chem., Int. Ed.* **2022**, *61*, No. e202111228.

(23) Novendra, N.; Marrett, J. M.; Katsenis, A. D.; Titi, H. M.; Arhangelskis, M.; Friščić, T.; Navrotsky, A. Linker Substituents Control the Thermodynamic Stability in Metal-Organic Frameworks. *J. Am. Chem. Soc.* **2020**, *142*, 21720−21729.

(24) Song, Y.; Feng, X.; Chen, J. S.; Brzezinski, C.; Xu, Z.; Lin, W. Multistep Engineering of Synergistic Catalysts in a Metal-Organic Framework for Tandem C-O Bond Cleavage. *J. Am. Chem. Soc.* **2020**, *142*, 4872−4882.

(25) Cai, G.; Jiang, H.-L. A Modulator-Induced Defect-Formation Strategy to Hierarchically Porous Metal−Organic Frameworks with High Stability. *Angew. Chem., Int. Ed.* **2017**, *56*, 563−567.

(26) Wang, K.; Feng, L.; Yan, T.; Wu, S.; Joseph, E. A.; Zhou, H. C. Rapid Generation of Hierarchically Porous Metal−Organic Frameworks through Laser Photolysis. *Angew. Chem., Int. Ed.* **2020**, *132*, 11445−11450.

(27) Feng, L.; Yuan, S.; Zhang, L. L.; Tan, K.; Li, J. L.; Kirchon, A.; Liu, L. M.; Zhang, P.; Han, Y.; Chabal, Y. J.; Zhou, H. C. Creating Hierarchical Pores by Controlled Linker Thermolysis in Multivariate Metal-Organic Frameworks. *J. Am. Chem. Soc.* **2018**, *140*, 2363−2372.

(28) Yuan, S.; Zou, L.; Qin, J. S.; Li, J.; Huang, L.; Feng, L.; Wang, X.; Bosch, M.; Alsalme, A.; Cagin, T.; Zhou, H. C. Construction of Hierarchically Porous Metal-Organic Frameworks through Linker Labilization. *Nat. Commun.* **2017**, *8*, 15356.

(29) Guillerm, V.; Xu, H.; Albalad, J.; Imaz, I.; Maspoch, D. Postsynthetic Selective Ligand Cleavage by Solid-Gas Phase

Ozonolysis Fuses Micropores into Mesopores in Metal-Organic Frameworks. *J. Am. Chem. Soc.* **2018**, *140*, 15022−15030.

(30) Yang, Y.; Arqué, X.; Patiño, T.; Guillerm, V.; Blersch, P. R.; Pérez-Carvajal, J.; Imaz, I.; Maspoch, D.; Sánchez, S. Enzyme-Powered Porous Micromotors Built from a Hierarchical Micro- And Mesoporous UiO-Type Metal-Organic Framework. *J. Am. Chem. Soc.* **2020**, *142*, 20962−20967.

(31) (a) Park, K. S.; Ni, Z.; Côté, A. P.; Choi, J. Y.; Huang, R.; Uribe-Romo, F. J.; Chae, H. K.; O'Keeffe, M.; Yaghi, O. M. Exceptional Chemical and Thermal Stability of Zeolitic Imidazolate Frameworks. *Proc. Natl. Acad. Sci. U.S.A.* **2006**, *103*, 10186−10191. (b) Huang, X. C.; Lin, Y. Y.; Zhang, J. P.; Chen, X. M. Ligand-directed strategy for zeolite-type metal−organic frameworks: zinc(II) imidazolates with unusual zeolitic topologies. *Angew. Chem., Int. Ed.* **2006**, *45*, 1557−1559.

(32) Phan, A.; Doonan, C. J.; Uribe-Romo, F. J.; Knobler, C. B.; O'Keeffe, M.; Yaghi, O. M. Synthesis, Structure, and Carbon Dioxide Capture Properties of Zeolitic Imidazolate Frameworks. *Acc. Chem. Res.* **2010**, *43*, 58−67.

(33) Banerjee, R.; Phan, A.; Wang, B.; Knobler, C.; Furukawa, H.; O'Keeffe, M.; Yaghi, O. M. High-Throughput Synthesis of Zeolitic Imidazolate Frameworks and Application to CO_2 Capture. *Science* **2008**, *319*, 939−943.

(34) Noh, K.; Lee, J.; Kim, J. Compositions and Structures of Zeolitic Imidazolate Frameworks. *Isr. J. Chem.* **2018**, *58*, 1075−1088.

(35) López-Cabrelles, J.; Romero, J.; Abellán, G.; Giménez-Marqués, M.; Palomino, M.; Valencia, S.; Rey, F.; Mínguez Espallargas, G. Solvent-Free Synthesis of ZIFs: A Route toward the Elusive Fe(II) Analogue of ZIF-8. *J. Am. Chem. Soc.* **2019**, *141*, 7173−7180.

(36) Feng, L.; Wang, K. Y.; Day, G. S.; Ryder, M. R.; Zhou, H. C. Destruction of Metal-Organic Frameworks: Positive and Negative Aspects of Stability and Lability. *Chem. Rev.* **2020**, *120*, 13087−13133.

(37) Ding, H. J.; Zhang, Y.; Wang, X.; Lin, Q. Y.; Zhang, S. M.; Yu, M. H.; Chang, Z.; Bu, X. H. Defective Hierarchical Pore Engineering of a Zn-Ni MOF by Labile Coordination Bonding Modulation. *Inorg. Chem.* **2021**, *60*, 5122−5130.

(38) Vitillo, J. G.; Gagliardi, L. Modeling Metal Influence on the Gate Opening in ZIF-8 Materials. *Chem. Mater.* **2021**, *33*, 4465−4473.

(39) Ambroz, F.; Macdonald, T. J.; Martis, V.; Parkin, I. P. Evaluation of the BET Theory for the Characterization of Meso and Microporous MOFs. *Small Methods* **2018**, *2*, No. 1800173.

(40) Wang, F.; Liu, Z. S.; Yang, H.; Tan, Y. X.; Zhang, J. Hybrid Zeolitic Imidazolate Frameworks with Catalytically Active TO 4 Building Blocks. *Angew. Chem., Int. Ed.* **2011**, *50*, 450−453.

(41) López-Cabrelles, J.; Miguel-Casañ, E.; Esteve-Rochina, M.; Andres-Garcia, E.; Vitórica-Yrezábal, I. J.; Calbo, J.; Mínguez Espallargas, G. Multivariate Sodalite Zeolitic Imidazolate Frameworks: A Direct Solvent-Free Synthesis. *Chem. Sci.* **2022**, *13*, 842−847.

(42) Butler, K. T.; Hendon, C. H.; Walsh, A. Designing Porous Electronic Thin-Film Devices: Band Offsets and Heteroepitaxy. *Faraday Discuss.* **2017**, *201*, 207−219.

(43) León-Alcaide, L.; Christensen, R. S.; Keen, D. A.; Jordá, J. L.; Brotons-Alcázar, I.; Forment-Aliaga, A.; Mínguez Espallargas, G. Meltable, Glass-Forming, Iron Zeolitic Imidazolate Framework. *J. Am. Chem. Soc.* **2023**, *145*, 11258−11264.

(44) Vitillo, J. G. Magnesium-Based Systems for Carbon Dioxide Capture, Storage and Recycling: From Leaves to Synthetic Nano-structured Materials. *RSC Adv.* **2015**, *5*, 36192−36239.

(45) Greenwood, N. N.; Gibb, T. C. *Mössbauer Spectroscopy*; Chapman and Hall: London, 1971.

(46) Both sextets with very low intensity have IS consistent with Fe^{3+}, one of them with high QS suggesting it is located on a very distorted site and corresponding to ca. 5% of the iron centres. The other one with lower QS consistent with superparamagnetic Fe^{3+} oxides as confirmed by te spectrum taken at 4 K. This is likely the result of a partial oxidation during the manipulation of the as-synthetized material..

(47) Murad, E. Clays and clay minerals: What can Mössbauer spectroscopy do to help understand them? *Hyperf. Interac.* **1998**, *117*, 39−70.

(48) Sheldrick, G. M. SHELXT − Integrated space-group and crystal-structure determination. *Acta Crystallogr.* **2015**, *71*, 3−8.

(49) Dolomanov, O. V.; Bourhis, L. J.; Gildea, R. J.; Howard, J. A. K.; Puschmann, H. OLEX2: A Complete Structure Solution, Refinement and Analysis Program. *J. Appl. Crystallogr.* **2009**, *42*, 339−341.

(50) Coelho, A. A. TOPAS and TOPAS-Academic: an optimization program integrating computer algebra and crystallographic objects written in C++. *J. Appl. Crystallogr.* **2018**, *51*, 210.

(51) Long, G. J.; Cranshaw, T. E.; Longworth, G. The ideal Mössbauer effect absorber thicknesses. *Mossb. Effect. Ref. Data J.* **1983**, *6*, 42−49.

(52) Blum, V.; Gehrke, R.; Hanke, F.; Havu, P.; Havu, V.; Ren, X.; Reuter, K.; Scheffler, M. Ab Initio Molecular Simulations with Numeric Atom-Centered Orbitals. *Comput. Phys. Commun.* **2009**, *180*, 2175−2196.

(53) Perdew, J. P.; Ruzsinszky, A.; Csonka, G. I.; Vydrov, O. A.; Scuseria, G. E.; Constantin, L. A.; Zhou, X.; Burke, K. Restoring the Density-Gradient Expansion for Exchange in Solids and Surfaces. *Phys. Rev. Lett.* **2008**, *100*, No. 136406.

(54) Heyd, J.; Scuseria, G. E.; Ernzerhof, M. Hybrid Functionals Based on a Screened Coulomb Potential. *J. Chem. Phys.* **2003**, *118*, 8207−8215.

(55) Bardeen, C. J. The Structure and Dynamics of Molecular Excitons. *Annu. Rev. Phys. Chem.* **2014**, *65*, 127−148.

(56) Nayak, P. K. Exciton Binding Energy in Small Organic Conjugated Molecule. *Synth. Met.* **2013**, *174*, 42−45.

(57) Frisch, M. J.; Trucks, G. W.; Schlegel, H. B.; Scuseria, G. E.; Robb, M. A.; Cheeseman, J. R.; Scalmani, G.; Barone, V.; Petersson, G. A.; Nakatsuji, H.; et al. *Guassian 16*, Revision A06; Gaussian, Inc.: Wallingford CT, 2016.

(58) Lefebvre, C.; Klein, J.; Khartabil, H.; Boisson, J.-C.; Hénon, E. IGMPlot: A program to identify, characterize, and quantify molecular interactions. *J. Comput. Chem.* **2023**, *44*, 1750−1756.

■ NOTE ADDED AFTER ASAP PUBLICATION

This paper was published on October 9, 2023. Figure 3 has been updated and the revised version of the paper was re-posted on October 11, 2023.